TOPICAL REVIEW— Magnetism, magnetic materials, and interdisciplinary research

Reactively sputtered Fe_3O_4-based films for spintronics*

Li Peng(李 鹏), Jin Chao(金 朝), Mi Wen-Bo(米文博), and Bai Hai-Li(白海力)†

Tianjin Key Laboratory of Low Dimensional Materials Physics and Preparing Technology, Institute of Advanced Materials Physics, Faculty of Science, Tianjin University, Tianjin 300072, China

(Received 1 March 2013)

Half metallic polycrystalline, epitaxial Fe_3O_4 films and Fe_3O_4-based heterostructures for spintronics were fabricated by DC reactive magnetron sputtering. Large tunneling magnetoresistance was found in the polycrystalline Fe_3O_4 films and attributed to the insulating grain boundaries. The pinning effect of the moments at the grain boundaries leads to a significant exchange bias. Frozen interfacial/surface moments induce weak saturation of the high-field magnetoresistance. The films show a moment rotation related butterfly-shaped magnetoresistance. It was found that in the films, natural growth defects, antiphase boundaries, and magnetocrystalline anisotropy play important roles in high-order anisotropic magnetoresistance. Spin injection from Fe_3O_4 films to semiconductive Si and ZnO was measured to be 45% and 28.5%, respectively. The positive magnetoresistance in the Fe_3O_4-based heterostructures is considered to be caused by a shift of the Fe_3O_4 $e_g\uparrow$ band near the interface. Enhanced magnetization was observed in $Fe_3O_4/BiFeO_3$ heterostructures experimentally and further proved by first principle calculations. The enhanced magnetization can be explained by spin moments of the thin $BiFeO_3$ layer substantially reversing into a ferromagnetic arrangement under a strong coupling that is principally induced by electronic orbital reconstruction at the interface.

Keywords: reactively sputtered Fe_3O_4 films, spintronics, magnetoresistance, interface

PACS: 75.47.–m, 72.25.Mk, 81.15.Cd, 85.75.–d **DOI:** 10.1088/1674-1056/22/4/047505

1. Introduction

Fe_3O_4 with a Néel transition temperature of $T_N = 858$ K is a mixed-valence compound with the tetrahedral (A) sublattice completely occupied by ferric ions, while in the octahedral (B) sublattice half of the sites are occupied by Fe^{2+} and the other half by Fe^{3+} ions. Below 858 K, Fe_3O_4 manifests ferrimagnetic features with A-site magnetic moments align antiparallel to the B-site moments. Crossing ~125 K, Fe_3O_4 undergoes a first-order phase transition (the Verwey transition), its crystal symmetry is lowered to monoclinic and its electrical conductivity drops by more than two orders of magnitude.[1]

An ancient and fascinating material, Fe_3O_4 has recently been investigated by many groups because of its half-metallic band structure.[2] Owing to its ideal 100% spin polarization at the Fermi level, Fe_3O_4 is promising in spintronic applications such as magnetic tunnel junctions,[3] spin injection heterostructures,[4] and spin valves.[5] The main fabrication techniques for Fe_3O_4 films are RF magnetron sputtering, molecular-beam epitaxy, and pulse-laser deposition. Hampered by difficulties in controlling the stoichiometry of Fe_3O_4, DC reactive sputtering is rarely reported in the literature, but it is much cheaper at an industrial scale than the other deposition techniques. Hence, motivated by spintronics applications, it is worth exploring the reactive sputtering fabrication of Fe_3O_4 films further through optimizing the deposition conditions.

It is important to note here that high spin polarization causes significant TMR, because TMR arises from spin-dependent tunneling between ferromagnetic (FM) particles of granular solids[6] or FM electrodes of tunnel junctions,[7] and is proportional to the spin polarization of the tunneling electrons.[8] Therefore, many research efforts have been focused on the MR in magnetites of different forms, including single crystals, epitaxial and polycrystalline films, powder, and electrodes on junctions.[9, 10, 11, 12, 13, 14] Nevertheless, the large MR that was anticipated was not observed in Fe_3O_4 polycrystalline films and powder compact, especially at room temperature. Generally, grain boundaries act as the tunneling barrier in polycrystalline Fe_3O_4 films. However, the physical mechanisms of the magnetic and transport properties of these films are still far from clear, especially the effects of moments at grain boundaries on its magnetic and transport properties, and increased insight in this area is crucial for understanding the magnetic and electrical transport properties of half-metallic films with grain boundaries, such as polycrystalline Fe_3O_4, SrFeMoO, and LaSrMnO films.

Owing to the relatively low spinel crystal symmetry of Fe_3O_4, intrinsic natural growth defects, antiphase boundaries (APBs), are usually observed in epitaxial Fe_3O_4 films on MgO, $SrTiO_3$, c-Al_2O_3, $MgAl_2O_4$, etc. The cation sublattice (Fe) is shifted $1/4a[110]$ with the anion sublattice (O) undistorted in Fe_3O_4. According to Sawatzky,[15] the exchange

*Project supported by the National Natural Science Foundation of China (Grant No. 51272174) and the Natural Science Foundation of Tianjin City (Grant No. 12JCYBJC11100).

†Corresponding author. E-mail: baihaili@tju.edu.cn

© 2013 Chinese Physical Society and IOP Publishing Ltd

integral J across the boundaries is proportional to $\cos^2\theta$, in which θ is the bond angle subtended by cation–anion–cation. The bond angles of iron–oxygen–iron across APBs in epitaxial Fe_3O_4 films are near 180° and strong antiferromagnetic couplings are formed.[16] This strong antiferromagnetic coupling across APBs has an obvious influence on the magnetic and transport properties.[16, 17] However, the physical mechanism of magnetoresistance and anisotropic magnetoresistance in epitaxial Fe_3O_4 films is still not clear, and understanding it is fundamental to the exploration of half-metals in spintronics.

Injection and detection of spin-polarized currents are crucial for spintronics. However, to apply a ferromagnetic metal in spintronics devices, one must overcome the conductivity mismatch between metals and semiconductors. Up to now, many experiments have indicated that the spin injection efficiency that can be achieved is less than 1%.[18, 19] It has recently been demonstrated that spin injection can be obtained by tunneling through a barrier at an interface[20, 21] or by employing a magnetic semiconductor.[22] Another approach is to use half-metallic ferromagnets such as Fe_3O_4.[23, 24] Furthermore, it is well known that the interface also plays an important role in the magnetic coupling and magnetoresistance of heterostructures, for instance, the exchange bias coupling in the Fe/Cr/Fe superlattice for giant magnetoresistance and giant tunneling magnetoresistance in polycrystalline $Zn_{0.41}Fe_{2.59}O_4$ with α-Fe_2O_3 boundaries.[25] Hence, exploration of the interfacial magnetic coupling and interface-related magnetoresistance of Fe_3O_4-based heterostructures with current perpendicular to the film plane is needed because of many anticipated practical applications.

In our work, the polycrystalline, epitaxial Fe_3O_4 films and Fe_3O_4-based heterostructures were fabricated by DC reactive sputtering. The magnetic and tunneling magnetoresistance in the polycrystalline Fe_3O_4 films is determined by the pinning effect of amorphous and insulating grain boundaries. The origin of butterfly-shaped magnetoresistance and high-order anisotropic magnetoresistance in epitaxial Fe_3O_4 films was revealed to be related to the APBs and magnetocrystalline anisotropy. The spin injection, magnetoresistance, and magnetic coupling of Fe_3O_4-based heterostructures were also found to be closely associated with the interface band structure and interfacial moment structures.

2. Experiments

Polycrystalline and epitaxial Fe_3O_4 films were fabricated by DC reactive magnetron sputtering from a pure Fe target in an atmosphere of Ar and O_2 with a base pressure greater than 8.0×10^{-6} Pa. The doped Fe_3O_4 films were fabricated by reactive cosputtering from a pure Fe target and other metal targets. The semiconductive Si, ZnO, and insulating MgO were deposited by RF sputtering. Several kinds of substrate, including amorphous glass, Kapton, single crystal silicon, NaCl, MgO, $SrTiO_3$, and c-Al_2O_3 with different orientations, were chosen to fabricate the single layer films and heterostructures. The film thickness was determined by a Dektak 6M surface profiler.

The microstructure of the samples was characterized by high-resolution transmission electron microscopy (HRTEM) and X-ray diffraction (XRD, Cu Kα source, $\lambda = 1.5406$ Å, 1 Å = 0.1 nm), including normal θ–2θ scan, tilting scan, φ scan, and pole figure scan. The topography and surface imaging were observed by scanning electron microscopy (SEM) and atomic force microscopy (AFM). The element contents were analyzed by energy-dispersive X-ray spectroscopy (EDS) equipment on a scanning electron microscope. The chemical state was analyzed by X-ray photoelectron spectroscopy (XPS) using Mg Kα radiation (1253.6 eV) and by laser micro-Raman spectroscopy.

The magnetic properties involving zero-field and field cooling (ZFC and FC) and M–H measurement were carried out by a quantum design physical property measurement system (VSM-PPMS) and a quantum design magnetic property measurement system (SQUID-VSM) at temperatures ranging from 5 K to 300 K. The magnetic anisotropy was studied by a vibrating sample magnetometer (VSM) with a sample rotator at room temperature.

The resistivity and magnetoresistance were measured in a standard four-probe configuration using a physical property measurement system (PPMS). The angular dependence of anisotropic magnetoresistance was measured by the standard four-probe configuration using the PPMS-9 equipped with a sample rotator. The current–voltage curves and magnetoresistance of heterostructures were investigated using the AC transport measurement of the PPMS-9.

3. Polycrystalline Fe_3O_4-based films

Figure 1(a) presents the XRD profile of a typical polycrystalline Fe_3O_4 film. The diffraction peaks and the relative intensities are completely consistent with those of polycrystalline Fe_3O_4 powders, implying an absence of textures in the film. It should be noted that γ-Fe_2O_3 (maghemite) has the same cubic inverse spinel structure and nearly the same lattice constant ($a = 0.8350$ nm) as those of Fe_3O_4 ($a = 0.8396$ nm). Therefore, the diffraction peaks cannot be uniquely indexed to Fe_3O_4, but γ-Fe_2O_3 must also be considered, along with their mixture. In order to clarify the phases presented in the film further, XPS measurements were performed to analyze the binding energy of Fe 2p. The Fe 2p core-level photoemission spectrum of the film taken at $h\nu = 1253.6$ eV is shown in Fig. 1(b). Due to the spin–orbit coupling, the Fe 2p core levels split into $2p_{1/2}$ and $2p_{3/2}$ components, situated at 711 eV and 724 eV, respectively. The broadening of the Fe $2p_{1/2}$ and

$2p_{3/2}$ peaks indicates the presence of Fe^{2+}. The satellite line situated at 719 eV, which is characteristic of the Fe^{3+} in γ-Fe_2O_3, is absent in the spectrum. Therefore, the suspected presence of γ-Fe_2O_3 is ruled out and the film is shown to be composed of pure Fe_3O_4.

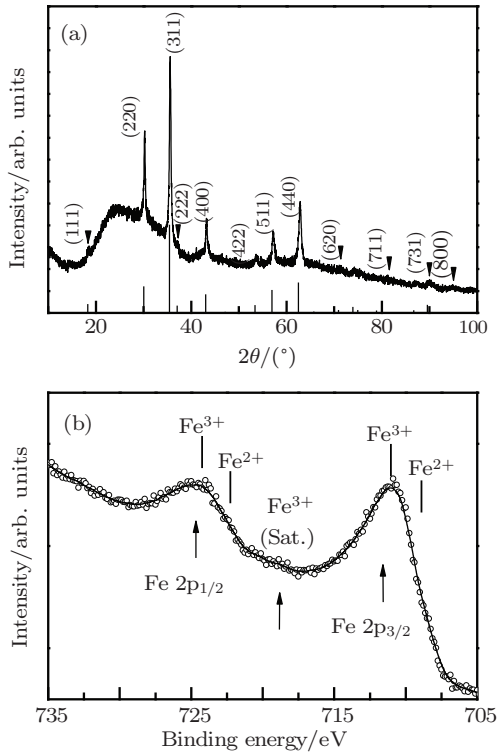


Fig. 1. Typical XRD profile (a) and XPS spectrum of Fe 2p (b) of a typical reactively sputtered polycrystalline Fe_3O_4 films.[26]

Figure 2(a) shows the bright field image and selected area diffraction (SAED) pattern of a 40-nm Fe_3O_4 film. One can see that the film is polycrystalline and Fe_3O_4 grains are well separated by grain boundaries. All the diffraction rings are from polycrystalline Fe_3O_4. The bottom inset of Fig. 2(a) gives the bright field image of 300-nm Fe_3O_4 film. By the linear intercept method, i.e. from the number of line crossings, the average lateral grain size was measured to be ~ 25 nm. Figure 2(b) shows the cross-sectional SEM image of the 330-nm Fe_3O_4 film, indicating a column structure.

In order to observe the microstructure of Fe_3O_4 grains and their boundaries directly, we collected the high-resolution TEM image of the 20-nm thick film, as shown in Fig. 3. From the TEM image one can determine that the average size of Fe_3O_4 grains is ~ 5 nm and these grains are surrounded by disordered atoms, or the shell structure. The presence of the disordered atoms can be ascribed to lattice mismatch between adjacent Fe_3O_4 grains with different lattice orientations and relaxations because of bond order deficiency. This disorder at grain boundaries has a great impact on the magnetic and magnetotransport properties.

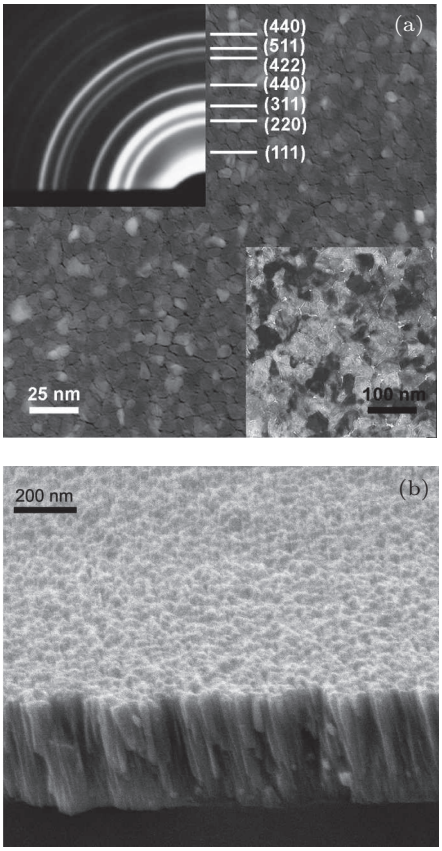


Fig. 2. (a) TEM bright field image and SAED pattern and (b) cross-sectional SEM image of Fe_3O_4 film.[27]

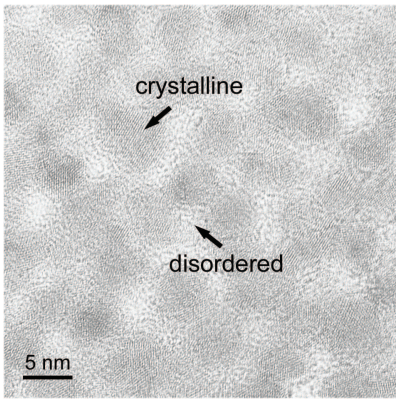


Fig. 3. Planar-view high resolution TEM image of the 20-nm polycrystalline Fe_3O_4 film.[26]

Figure 4 shows the zero-field cooled (ZFC) and field cooled (FC) magnetization curves for the polycrystalline Fe_3O_4 film recorded at a field of 300 Oe (1 Oe = 79.5775 A/m). The abrupt changes in the ZFC and FC curves around 110 K correspond to the Verwey transition (T_V). This Verwey transition temperature is slightly lower than 125 K that is characteristic of single crystalline Fe_3O_4 samples. The reduction in T_V has been ascribed to Fe vacancies on the B sites and interfacial strain.[28] The appearance of Fe vacancies on the B sites decreases the exchange interaction among the Fe ions located at the B sites and therefore decreases the T_V.

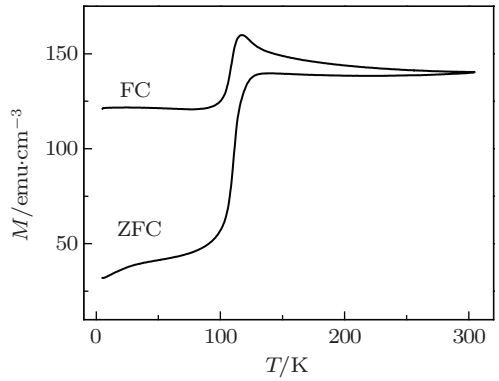


Fig. 4. Typical temperature dependence of zero field cooling and field cooling magnetization of polycrystalline Fe_3O_4 films.

Figure 5 shows the field cooling M–H curves of the film measured at 80 K and the temperature dependence of both coercivity (H_C) and the exchange bias field (H_E). From Fig. 5(a), one can see that the first hysteresis loop shifts to a negative orientation along the H axis. Meanwhile, the magnetization at 2 kOe is higher than that at −2 kOe. In the fourth loop, the shift disappears, indicating a training effect. Furthermore, all the loops are open in a field up to 50 kOe due to high-field irreversibility. The H_E ($= |H_C + H_C|/2$) of the M–H loop of the 640-nm thick film, measured at 80 K for the first time, is 100 Oe in a 50-kOe field. The same phenomenon has also been observed in epitaxial Fe_3O_4 films and in the Fe–Fe_2O_3 composite system.[29, 30] The temperature dependence of H_E and H_C in Fig. 5(b), derived from the FC hysteresis loops measured at each temperature, indicates that both H_E and H_C decrease with the increase of temperature. The magnitude of H_C shows a gradual increase with the decrease of temperature and a sharp increase when the sample is cooled below T_V. The magnitude of H_E exhibits a temperature dependence similar to that of H_C. The magnitude of H_E depends strongly on the thermomagnetic history of the sample. The strong increase in H_C below the T_V is due to the associated structural phase transition from cubic to monoclinic phase and subsequent changes in anisotropy constants.

A system displaying exchange bias must contain, at least, two exchange coupled phases: one is the reversible phase and the other is the fixed phase in the field range of measurements. However, in the pure polycrystalline Fe_3O_4 system, there is no secondary fixed phase in the film and, therefore, it may be that the spin-glass-like phase with high-field irreversibility at the Fe_3O_4 grain boundaries plays the role of the fixed phase. According to the above analyses of the ZFC and FC curves measured in a 50-kOe field, we can deduce that the disordered spins at the grain boundaries are the main source of exchanging bias, as has been observed in the Fe–Fe_2O_3 system.[30] When the system is cooled down to a temperature below the spin frozen temperature (T_f) in an external field, some of the spins of the spin-glass-like phase are aligned to and frozen in the direction of the cooling field. In the subsequent hysteresis loop measurements, some of the frozen spins keep their directions and provide a pinning force to the reversible spins. As a result, exchange bias appears. The schematic diagram of the spin configuration of a single Fe_3O_4 grain during magnetizing is shown in Fig. 6.

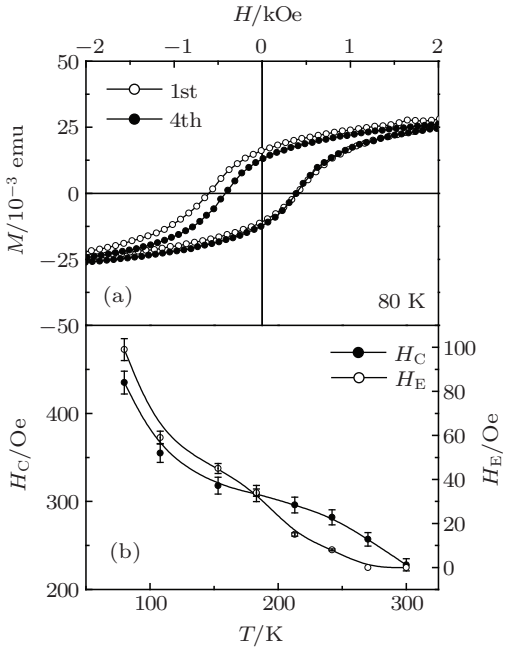


Fig. 5. (a) Field-cooled M–H curves of the polycrystalline Fe_3O_4 film at 80 K. (b) Temperature dependence of coercivity (H_C) and exchange bias field (H_E).[26]

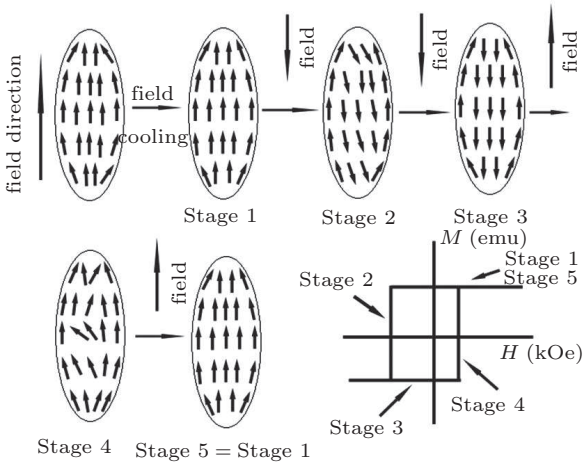


Fig. 6. Schematic diagram of the spin configuration of a single Fe_3O_4 grain during the magnetizing process.[26]

Figure 7 shows the MR of polycrystalline Fe_3O_4 films (defined as MR$= (\rho_H - \rho_0)/\rho_0$) as a function of applied magnetic field, parallel and perpendicular to the film plane, for the 330-nm-thick sample at room temperature. Also shown in the figure are the normalized parallel and perpendicular MR at different temperatures, and the low field ($H < 10$ kOe) MR. Several features in this figure are quite noteworthy. (i) At

50 kOe, the parallel MR is 7.4%, larger than perpendicular MR of 5.8%, a very large value for an Fe_3O_4 material at RT. (ii) Under low fields, the perpendicular MR shows quadratic behavior up to 5 kOe, whereas the parallel MR is nearly linear in this regime. (iii) The normalized MR is independent of temperature and shows a very weak saturation trend as the magnetic field increases to 50 kOe.

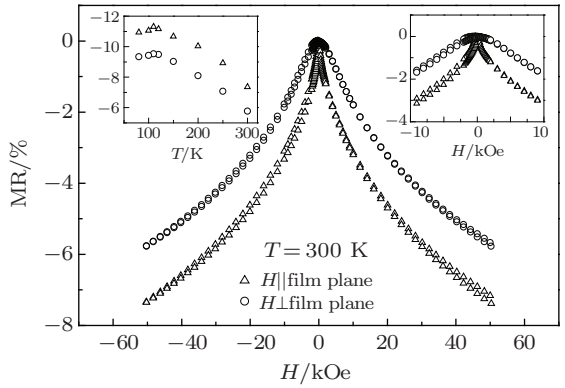


Fig. 7. Parallel and perpendicular MR measured at 300 K. Insets show normalized MR at different temperatures (left) and low-field MR (right).[27]

In granular systems with negligible intergrain interaction,[31] MR is closely correlated with magnetization and can be described by $\mathrm{MR} = \Delta\rho/\rho_0 \propto -(M/M_S)^2$. As clearly shown in Fig. 7, this relation is not followed by our Fe_3O_4 granular system. This implies that a correlation effect of adjacent grains must be taken into account when we attempt to explain the observed interesting behaviors of MR, as illustrated schematically in Fig. 8. Based on the tunneling electrical properties of polycrystalline Fe_3O_4 films (not shown), we can conclude that when a magnetic field is applied, the spins in the central regions of the grains are oriented first, while the spins at the surface are only slightly affected. As the magnetic field is increased above the field at which the spins at the grain boundaries start to become aligned, resistance decreases abruptly because only the interfacial/surface spins determine the tunneling probability. The schematic diagram of the tunneling process between two Fe_3O_4 grains is shown in Fig. 8.

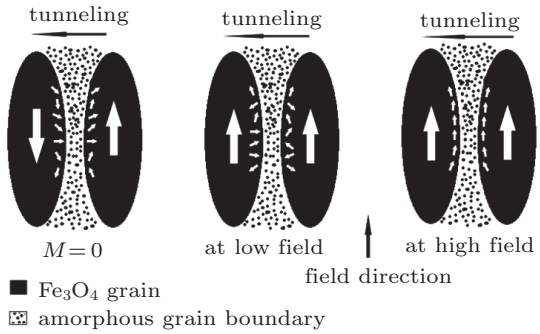


Fig. 8. Schematic illustration of the tunneling process between two Fe_3O_4 grains.[26]

4. Epitaxial Fe_3O_4-based films

The typical XRD θ–2θ pattern of Fe_3O_4 films is given in Fig. 9(a). Bulk Fe_3O_4 has an inverse spinel structure with a lattice constant of $a_{Fe_3O_4} = 8.394$ Å and MgO has a face-centered cubic structure with a lattice constant of $a_{MgO} = 4.212$ Å, giving a small lattice mismatch of $(a_{Fe_3O_4} - 2a_{MgO})/2a_{MgO} = -0.4\%$. The XRD pattern reveals that the film grows along the (100) orientation. However, the orientation does not imply epitaxy because sputtered films always show a columnar structure. On the other hand, most of the diffraction peaks from Fe_3O_4 and MgO overlap, and their distinction lies in the absence of (111) and (220) peaks for MgO. Hence tilting 2θ scans were performed to further clarify the structure, as shown in the right inset of Fig. 9(a). The tilting XRD patterns exhibit Fe_3O_4 (220) ($\alpha = 45°$, $\beta = 0°$) and (111) ($\alpha = 35.3°$, $\beta = 45°$) exclusively, suggesting in-plane epitaxy. The pole-figure collected at $2\theta = 18.3°$ is shown in the left inset of Fig. 9(a), which displays four very strong sharp spots corresponding to {111} planes, without other distinct spots or rings observed. To further confirm the epitaxial structure, φ scans were performed at $\alpha = 35.3°$, as shown in Fig. 9(b). The interval of four peaks is exactly 90°, indicating fourfold symmetry. From the above XRD analyses, we can conclude that the epitaxial relationship is $Fe_3O_4(004)[100] \parallel MgO(002)[100]$.

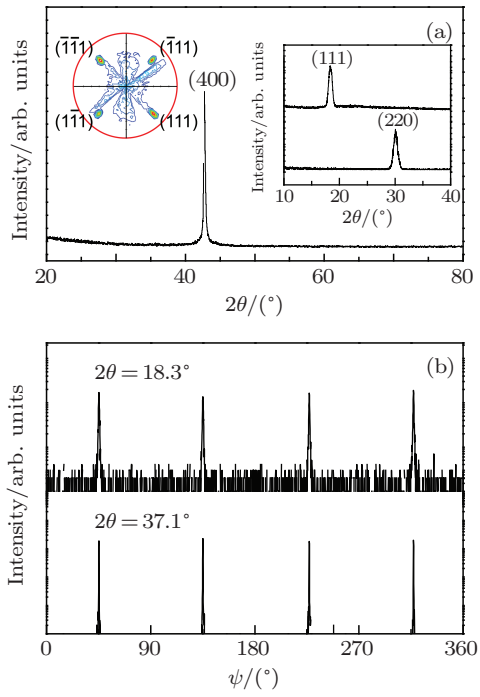


Fig. 9. XRD patterns of the 240-nm thick epitaxial Fe_3O_4 films: (a) conventional θ–2θ scan, and (b) φ scans. Inset in panel (a) shows the tilting 2θ scans (right) and pole figure (left).[32]

Figure 10(a) displays a cross sectional TEM image of the epitaxial Fe_3O_4 (001) films on MgO (001). The interface between MgO and Fe_3O_4 and the surface of Fe_3O_4 are rather flat and smooth. The cross sectional HRTEM of the Fe_3O_4/MgO

bilayers is given in Fig. 10(b), confirming the epitaxial heterostructure. The epitaxial relationship is further verified to be $Fe_3O_4(004)[100] \parallel MgO(002)[100]$. The inset in Fig. 10(b) gives the superimposed selected area electron diffraction spots from the interface of Fe_3O_4 (400) and MgO (200), indicating the epitaxial relationship and the small lattice mismatch ($\sim 0.3\%$) further. Figure 10(c) displays the HRTEM of the epitaxial Fe_3O_4 films, illustrating the presence of APBs due to the different crystal symmetry of MgO and Fe_3O_4. The cation sublattice has shifted $1/4a[110]$ with the anion sublattice undistorted in Fe_3O_4.

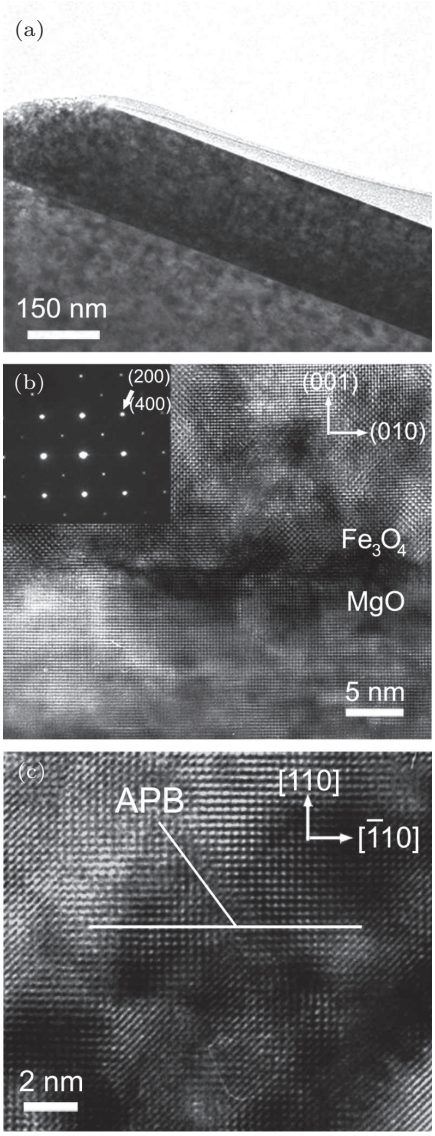


Fig. 10. Typical TEM images of epitaxial Fe_3O_4 films on MgO (001): (a) low resolution cross section, (b) high resolution cross section near interface, (c) antiphase boundaries.[33, 34]

Figure 11(a) displays the low-field MR–H relation which shows a butterfly shape. The high-field MR nearly yields linear dependence of H, as given in Fig. 11(b). Obviously, the relationship $\mathrm{MR} \propto (M_S/M)^2$, used to describe non-interacting granular systems, which usually gives a butterfly-shaped MR, is not suitable for the epitaxial Fe_3O_4 film.[35] According to Margulies *et al.*,[16, 17] the magnetization of epitaxial Fe_3O_4 films changes faster at low fields and is hard to saturate at high fields due to the antiferromagnetic coupling across APBs. This is indeed what we observed in our epitaxial Fe_3O_4 films (see Fig. 11(b)). It is therefore reasonable to assume that at low fields the moments far away from the APBs primarily orient to the magnetic field, and the transport can be treated as the hopping between two Fe_3O_4 grains weakly coupled across APBs. At high magnetic field, the moments near the APBs gradually align at high fields, and the transport can be considered as the hopping across a series of strongly coupled spins, similar to the spin chain model proposed by Eerenstein *et al.*[9] The orientations of spins under different fields are schematically shown in Fig. 12.

The conductance of Fe_3O_4 is dominated by a small-polaron (SP) mechanism, and the DC conductance can be expressed as $\sigma_{DC} = \sigma_{SP} \propto t^2 e^{-U/2kT}$,[36] where $t \propto \cos(\varphi/2)$ is the transfer integral[9] (φ: the angle between adjacent moments) and U stands for activation energy. MR is thus given by

$$\begin{aligned} \mathrm{MR} &= \frac{[\sigma_{SP}(H,T) - \sigma_{SP}(H_C,T)]}{\sigma_{SP}(H_C,T)} \propto \sigma_{SP}(H,T) \\ &\propto t^2 e^{-U/2kT}. \end{aligned} \tag{1}$$

At low fields, the conductance of a granular system is affected by the magnetic exchange energy $E_M \propto (M/M_S)^2$.[35] Together with the small-polaron conductance, the conductance of epitaxial Fe_3O_4 films can be expressed as

$$\begin{aligned} \sigma_h(H,T) \propto t^2 \Bigg\{ &\frac{1}{2}(1+P)\exp\left[-\frac{U+E_M}{2kT}\right] \\ &+ \frac{1}{2}(1-P)\exp\left[-\frac{U-E_M}{2kT}\right]\Bigg\}. \end{aligned} \tag{2}$$

P is the spin polarization and M_S the saturation magnetization. Making the Taylor series expansion for Eq. (2) and combining Eq. (1), we get

$$\mathrm{MR} \propto \sum_i A_i (M/M_S)^{2i}, \tag{3}$$

where A_i is the coefficient for different terms. In the low-field region, the $\Delta M/M_S$ ($\Delta M/M_S < 1$) related to ΔH in a weak interaction system is much smaller than that of epitaxial Fe_3O_4 films, so high-order terms $(\Delta M/M_S)^{2i}$ ($i \geq 2$) quickly approach zero and can be ignored. Whereas in epitaxial Fe_3O_4 films, high-order terms have to be retained due to the fast rotation of the spins far away from APBs. As shown in Fig. 11(a), MR–H curve can be well fitted by Eq. (3) at low fields.

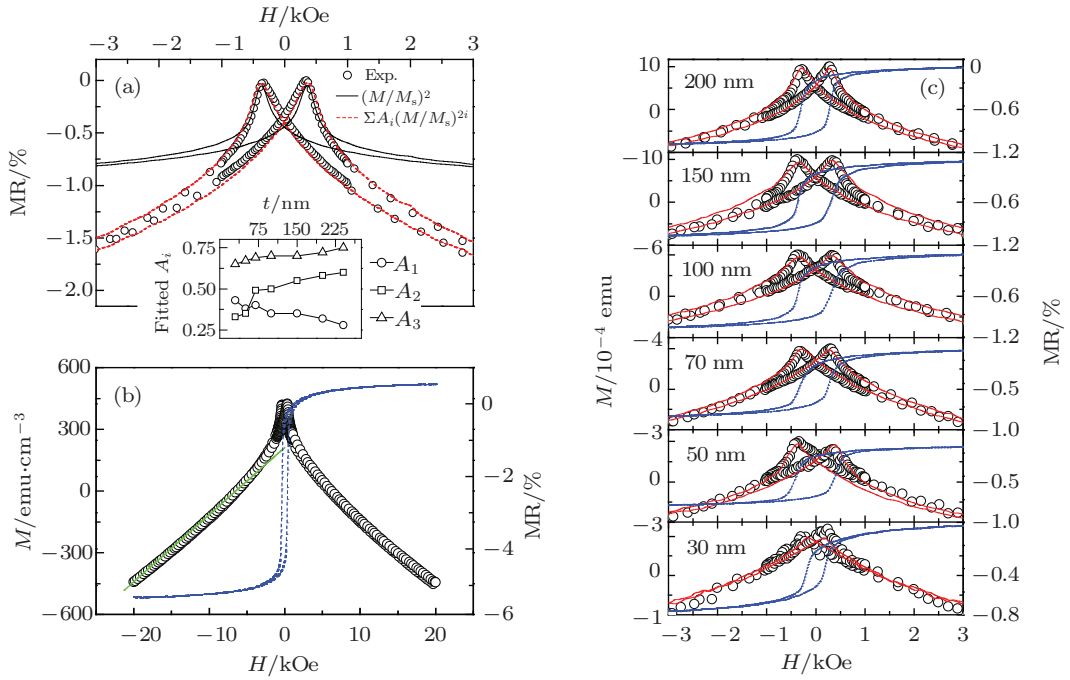


Fig. 11. (a) Low-field MR at 70 K for the 240-nm thick epitaxial Fe_3O_4 films and its fitting curves (dashed line) $\sum A_i(M/M_S)^{2i} = -0.28(M/M_S)^2 - 0.60(M/M_S)^4 - 0.75(M/M_S)^6$, and the inset is the fitted parameters A_i ($i = 1, 2, 3$) as a function of film thickness at 70 K. (b) Hysteresis loop (dashed line) and full MR curve at 70 K for the 240-nm thick epitaxial Fe_3O_4 films and its linear fitting. (c) Hysteresis loop (dashed line), measured MR (open circles) and the fitting curves of MR for the films with different thicknesses at 70 K.[32]

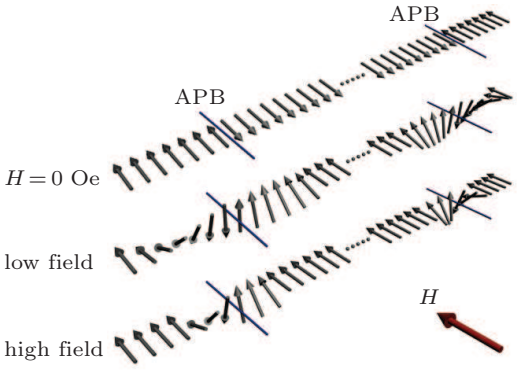


Fig. 12. Schematic diagram of the rotation of the spins near to and far away from APBs.[32]

The double-peak feature of MR observed here is consistent with the results of Ziese *et al.*; however, one-peak MR was observed by Eerenstein *et al*. It was speculated that the single peak of MR is caused by the large interval of measurement at low fields.[9, 37] Furthermore, the feature of double peaks is not so obvious for thinner films (Fig. 11(c)). The fitted parameter A_1 decreases and A_2, A_3 increase with increasing film thickness, as presented in the inset of Fig. 11(a). With the increase of film thickness, the size of antiphase domains increases,[38] resulting in a relatively larger contribution to magnetization at low fields by the ferromagnetic grains that are far away from APBs . Hence the larger A_i ($i \geq 2$) is needed to describe the MR behaviors (see the inset of Fig. 11(a)). With the increase of temperature, noise appears in the butterfly-shaped MR–H curves due to the thermal fluctuation of $(\Delta M/M_S)^{2i}$ (not shown).

In the high-field region, the spins near the APBs will align gradually to minimize the total energy of the system (see Fig. 12), which is generally considered to be composed of Zeeman energy E_H, exchange energy E_{ex}, and pinning energy E_{AF}. But for epitaxial Fe_3O_4 films, especially at low temperatures, magnetocrystalline anisotropy energy E_K must be considered. Experimentally, we applied H along $\langle 100 \rangle$, so $E_K = K\cos^2\varphi\sin^2\varphi = K\cos^2\varphi(1-\cos^2\varphi)$,[39] where K is the anisotropy constant and φ is the angle between M_S and H. The half energy density beside the APBs is

$$E_{left} = \int_{-l}^{0}\left[-M_S H\cos\varphi + K\cos^2\varphi(1-\cos^2\varphi) + A_F\left(\frac{d\varphi}{dx}\right)^2\right]dx, \quad (4)$$

where A_F represents ferromagnetic exchange stiffness and l stands for the gradual rotation region in Fig. 12. We thus get $E_{total} = E_{left} + E_{right} + A_{AF}[1-\cos(\varphi_2-\varphi_1)]/l$, where φ_1 (φ_2) is the angle between the magnetic field and left (right) spins across the APBs. With variational calculus and taking the equilibrium condition into consideration, $\partial E_{totalt}/\partial\varphi_1 = \partial E_{totalt}/\partial\varphi_2 = 0$, we get $\varphi_1 = -\varphi_2 = \varphi_{AF}/2$. Further, we obtain $(A_{AF}^2/A_F l^2 - K)(\cos^2\varphi_{AF} + \cos^3\varphi_{AF}) = M_S H$. We must pay attention to the E_K below T_V because a structural transition occurs at T_V. Below T_V, $E_K = K_1\cos^2\varphi + K_{11}\cos^4\varphi$.

($K_1 \gg K_{11}$).[40] We can get a similar expression approximately for $T < T_V$. Neglecting the cubic term $\cos^3 \varphi_{AF}$ and together with Eq. (1), we obtain

$$\mathrm{MR} \propto \cos^2 \varphi_{AF} \propto \frac{M_S H}{(A_{AF}^2/A_F l^2) - K}. \quad (5)$$

From Eq. (5), one can see that MR at high fields should change linearly with H, which is just what we observed in Fig. 11(b).

The temperature dependence of MR below T_V can also be qualitatively explained by Eq. (5). It can be seen that the MR of the epitaxial Fe_3O_4 film increases with decreasing T, especially below T_V (see Fig. 13). From Eq. (5), one can see that MR is enhanced with the decrease of T because the anisotropy constant K increases with decreasing T.[39, 40] K fitted by Eq. (5) is basically consistent with the corresponding reference data in the measuring temperature range,[39, 40] as presented in the inset of Fig. 13. In contrast, the tendency that MR increases with decreasing T below T_V is absent for the polycrystalline film due to its isotropy. The increase of MR below T_V in the epitaxial films can be understood by the fact that the cubic magnetocrystalline anisotropy field becomes larger at lower temperatures and consequently the moments are more inclined to align themselves along the easy axis ⟨100⟩. Hence the scattering induced by rotated spins becomes weaker under the applied field, leading to an increase in MR.

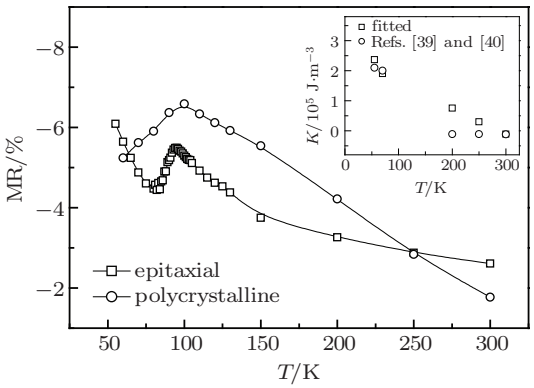


Fig. 13. MR–T curves for the epitaxial and polycrystalline Fe_3O_4 films. The inset shows the comparison of fitted anisotropy constant K and reference data.[32]

Since the magnetocrystalline anisotropy (E_K) has a great impact on the magnetotransport properties, it is reasonable to speculate that there is a close relation between E_K and anisotropic magnetoresistance.

Figure 14 gives the field dependence of MR of (001)-oriented films with different φ between the magnetic field and current. It is obvious that all the MR curves at different φ show the weak saturation tendency, and the MR exhibits two-fold symmetry at low fields and evolves to four-fold symmetry at high fields. The weak saturation of MR in epitaxial Fe_3O_4 films is caused by APBs.[9, 32] At $H = 20$ kOe, the weak saturated MR oscillates between -2.3% and -3.3%. It is therefore natural to assert that the high-field four-fold symmetric AMR not only correlates with the scattering center of APBs, but also some other factors that modify the MR at high fields.

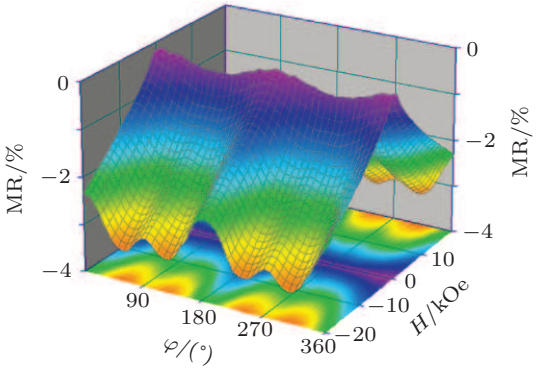


Fig. 14. Field dependence of angle-dependent MR for (001)-oriented epitaxial Fe_3O_4 film at 70 K.[41]

The two-fold symmetric AMR evolves to four-fold symmetry with the increase of magnetic field, as displayed in Figs. 14 and 15(a). To further explore the origins of the two-fold and four-fold symmetric AMR, the angular dependence of AMR can be fitted by

$$\mathrm{AMR} = P_1 + P_2 \cos(2\varphi + \varphi_0) + P_4 \cos(4\varphi + \varphi_0), \quad (6)$$

where P_2 and P_4 represent the amplitudes of two-fold and four-fold symmetric AMR, respectively. Considering the fact that it is difficult for the moments in epitaxial Fe_3O_4 films to become oriented along the direction of external field completely,[16] here φ is the angle between current and magnetic field rather than magnetization, and φ_0 is the misalignment at the beginning due to the gear clearance of the sample rotator. It is found that the field dependencies of P_2 and P_4 resemble those of magnetization[16] and magnetoresistance[9, 32] in the epitaxial Fe_3O_4 films, respectively, as given in Fig. 15(b).

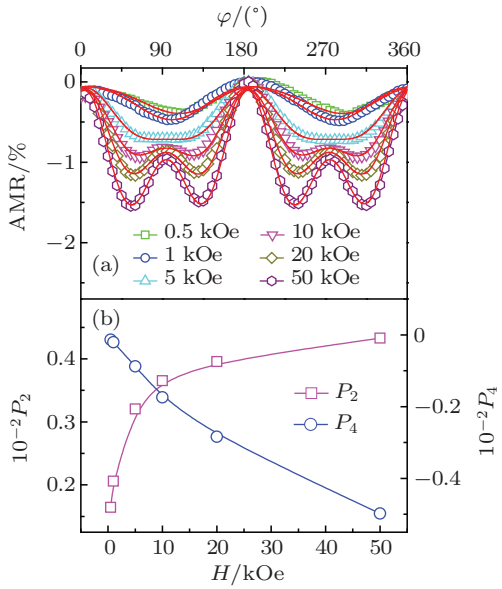


Fig. 15. (a) AMR for the epitaxial Fe_3O_4 films on MgO (001) at different magnetic fields ($T = 70$ K), and the red lines are the fitting curves of AMR. (b) Field dependence of fitting parameters P_2 and P_4.[34]

The anomalous four-fold symmetric anisotropic magnetoresistance has been supposed to be caused by the charge order of Fe^{2+} and Fe^{3+} on octahedral-site below Verwey transition temperature.[42] The charge order in magnetite can be destroyed by doping because Ni^{2+} is more inclined to occupy octahedral sites in spinel structure.[43, 44] Figure 16 displays the AMR of the epitaxial $Ni_{0.3}Fe_{2.7}O_4$ film under 50 kOe. It is clear that the four-fold AMR in the epitaxial $Ni_{0.3}Fe_{2.7}O_4$ film is maintained while the temperature increases up to 250 K, indicating that the four-fold AMR is not closely related to the charge order effect.[42]

In order to verify the relationship between high order symmetric AMR and magnetocrystalline anisotropy, AMR was investigated in epitaxial Fe_3O_4 (111) films at low temperatures ($T < T_V$) and in $Co_{0.6}Fe_{2.4}O_4$ (111) films. As displayed in Fig. 17(a)–17(c), six-fold symmetric AMR was observed at low temperature ($T < 50$ K) in Fe_3O_4 (111)/ZnO (0001) bilayers with current perpendicular to the film plane and a magnetic field in the film plane. It also can be seen that six-fold AMR nearly disappears due to the shift of easy axis from $\langle 100 \rangle$ to $\langle 111 \rangle$ while the temperature is larger than 100 K. And the six-fold term retains insaturation and increases with the magnetic field (Fig. 17(d)), which resembles the field dependence of the in-plane four-fold symmetric AMR in epitaxial Fe_3O_4 films. Furthermore, the six-fold symmetric AMR of the $Co_xFe_{3-x}O_4$ films was also observed at 140 K,[46] exhibiting an enhancement of the six-fold feature with increasing x. This characteristic is consistent with the increasing K_1 of $Co_xFe_{3-x}O_4$ with increasing x.[47, 48] Hence, the enhanced six-fold characteristic can be ascribed to the increased magnetocrystalline anisotropy with Co doping.

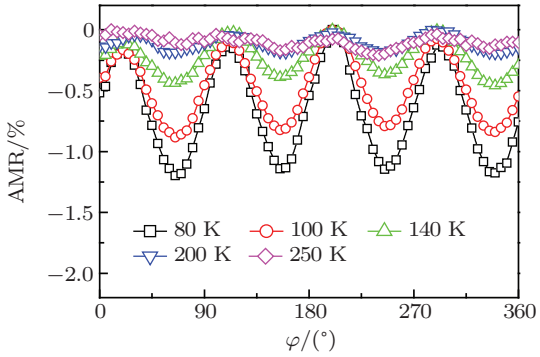


Fig. 16. AMR for the epitaxial $Ni_{0.3}Fe_{2.7}O_4$ thin films measured at different temperatures.[34]

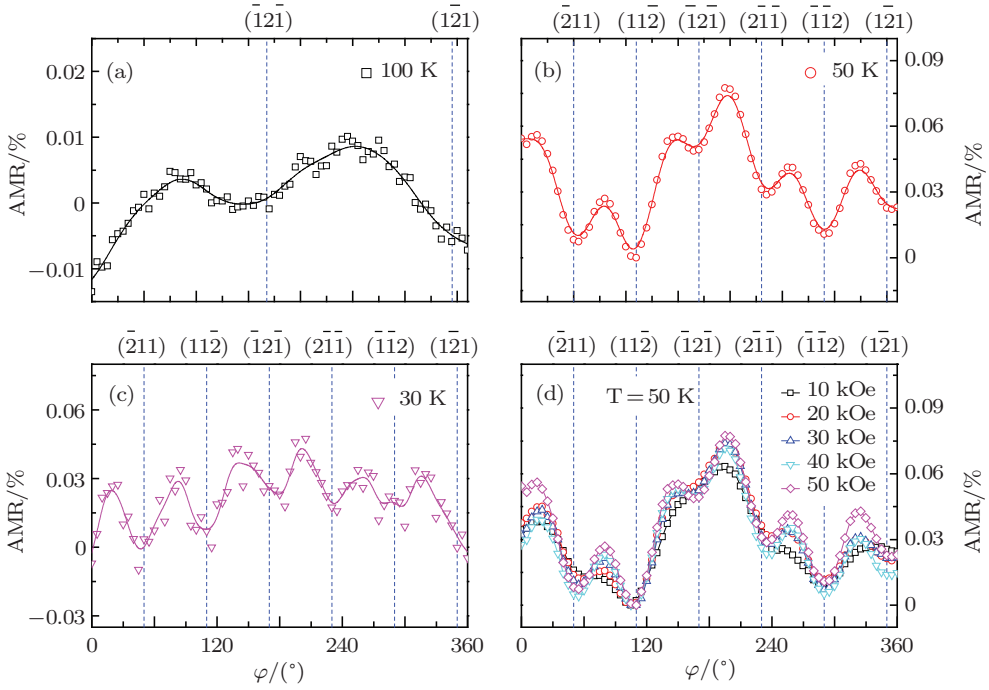


Fig. 17. Angular dependence of AMR for the Fe_3O_4 (111) films on ZnO (0001) measured at $H = 50$ kOe with different temperatures, (a) 100 K, (b) 50 K, (c) 30 K, and (d) AMR for the Fe_3O_4 (111) films on ZnO (0001) measured at different magnetic fields ($T = 50$ K). The solid lines are simply guides for the eyes.[45]

Therefore, it should be noted that the properties of epitaxial Fe_3O_4 films that differ from those of bulk are attributable to the antiferromagnetic coupling across the APBs, whereas such growth defects do not exist in manganite films. For instance, the hysteresis loop of epitaxial Fe_3O_4 films saturates much more slowly than that of epitaxial manganite films, due to the antiferromagnetic coupling.[16, 17, 49, 50] Under fields weaker than the magnetocrystalline anisotropy field ($H < H_K$), the spin-polarized electrons in manganite films exhibit a different scattering probability caused by the cubic magnetocrystalline

anisotropy. And the four-fold symmetric AMR evolves to two-fold because the cubic magnetocrystalline anisotropy field is overwhelmed by external magnetic fields. Nevertheless, the APBs act as the scattering center at high fields in the epitaxial Fe_3O_4 films.[9, 16, 17] At low fields, the moments far away from APBs primarily orient to the direction of the magnetic field and the scattering is mainly caused by the relative orientation of the moments far away from APBs.[32] While the magnetic field rotates in the film plane, the moments far away from APBs are always parallel to the magnetic field, causing the two-fold AMR. At high fields, the scattering is focused at APBs. The cubic magnetocrystalline anisotropy field superimposed onto the magnetic field further aligns the spin moments near APBs, resulting in an additional sinusoidal oscillation in scattering probability for the transport electrons along the hard or easy magnetization directions.

5. Fe_3O_4-based heterostructures

Several types of semiconductors, including amorphous Si, ZnO, and Nb:$SrTiO_3$, were adopted to investigate the spin injection of half metallic Fe_3O_4 films and spin related anisotropic magnetotransport properties.

ZnO, a wide band gap semiconductor with a hexagonal wurtzite structure, is a versatile material that has attracted attention due to its applications in light-emitting devices,[51, 52] transparent conductive oxide films,[53] room temperature diluted magnetic semiconductors in spintronics devices,[54] and so on. So the all-oxide Fe_3O_4/ZnO heterostructures is especially attractive due to the potential for spin injection into ZnO,[55] which is promising in the optical and spintronic fields.[56]

Figure 18(a) shows the I–V curves of the Fe_3O_4/ZnO heterostructure at different temperatures. The bottom left inset of Fig. 18(a) gives the schematic diagram of the four-probe measurement. The contact between Fe_3O_4 and ZnO is nearly Ohmic at temperatures higher than 30 K. The nonlinear rectifying property is observed at low temperatures, as ~ 0.8 V positive bias is obtained for 0.01 mA current and ~ -1.0 V is observed for -0.01 mA current. With a decrease of temperature ($T < 30$ K), a Schottky barrier forms at the interface, which is beneficial for the spin injection from ferromagnets into semiconductors. And the transport mechanism across the Schottky barrier is concluded to be thermal emission from the linear relation of $\lg|I| \sim V$, as displayed in the top left inset of Fig. 18(a). Sze[57] reported that the barrier height (Φ_B) of the heterostructure can be obtained from an activation energy plot, for which it is not necessary to specify the Richardson constant A^{**} or the junction area A_e. The slope of the data plotted as $\ln(I/T^2)$ versus $1/T$ at a given forward bias V yields the Φ_B via the relation

$$\ln(I/T^2) = \ln(A_e A^{**}) - \frac{q(\Phi_B - V)}{kT}. \tag{7}$$

Figure 18(b) shows the linear relationship of $\ln(I/T^2) \sim 1/T$ at 0.5 V bias, and the barrier height was calculated to be 0.51 eV at low temperatures, according to Eq. (7). The absolute value of spin polarization $|P|$ at different temperatures was also gained with the relation, as pointed out in a recent model proposed by Ziese *et al.*:[58]

$$I(B) = I(0)\left[1 + |P|\left(\frac{\mu_B B}{kT}\right) + \left(\frac{\mu_B B}{kT}\right)^2\right]. \tag{8}$$

The inset of Fig. 18(b) displays the relation of $I(B)/I(0)$ versus magnetic field at a bias of 0.08 V. Hence the transport of the spin polarization of epitaxial Fe_3O_4 films into epitaxial ZnO films can be obtained through linear fitting, according to Eq. (8). At high temperatures, the transport of the spin polarization of Fe_3O_4 into ZnO is zero due to the Ohmic contact at the interface. At 30 K, a spin polarization $P = 28.5\%$ was attained. A similar spin injection efficiency through a Schottky barrier from polycrystalline Fe_3O_4 films into amorphous silicon was also determined to be $\sim 45\%$ at 110 K.[4] It should be noted that the spin injection efficiency in Fig. 18 is much smaller than the ideal value of 100%. Possible causes for the smaller spin polarization are: i) The APBs certainly lead to a

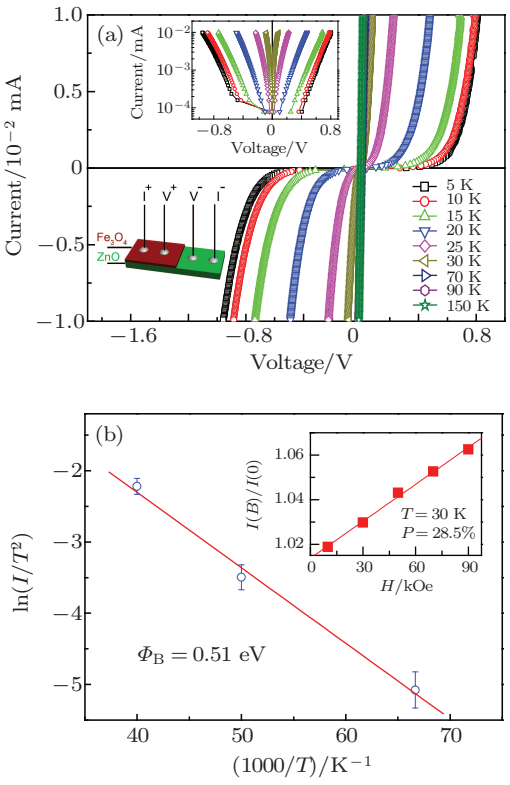


Fig. 18. (a) Current–voltage curves of Fe_3O_4 (111)/ZnO (0001) at different temperatures. Left top inset shows $\log I \sim V$ curves. (b) Linear fit to activation energy plot at a constant bias voltage. Inset is plot of $I(B)/I(0)$ versus applied magnetic field at 30 K.[59]

very large decrease in the spin polarization. ii) It is possible that defects at the interface, including lattice distortion and ion vacancies, result in the decrease of spin polarization.

To demonstrate the anisotropic transport properties across the interface, Figure 19 displays the measured angular dependence of AMR across the interface at $T = 90$ K for the Fe_3O_4/Nb(0.7 wt%):$SrTiO_3$ heterostructure, which is defined as AMR $= (\rho - \rho_{\bar{1}10})/\rho_{\bar{1}10}$. The AMR found in the Schottky barrier-based heterostructure is quite interesting and two important features are noticeable. First, the AMR across Schottky barrier is four-fold symmetric and rather large ($\sim 80\%$) at a critical bias ($I \sim 0.110$ mA). The four-fold symmetric feature is similar to that observed in the AMR of magnetite monolayers.[34, 41] In addition, absolute resistance change ΔR of the heterostructures ($\Delta R = R_{max} - R_{min}$) caused by the variation of φ is 10 Ω ∼ 20 Ω, which is also much larger than that of magnetite monolayer (90 K × AMR $\sim 10^{-6}$ Ω). Second, a 45° phase shift exists for the AMR–φ curves at currents below and above the critical current (~ 0.110 mA) at which AMR reaches its maximum value.

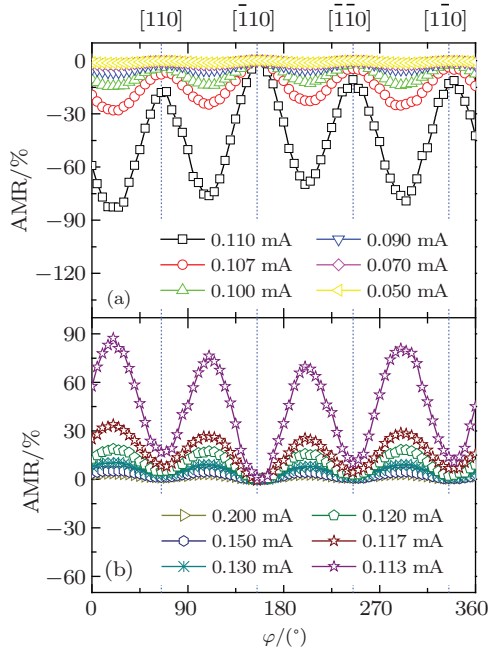


Fig. 19. AMR across the interface between Fe_3O_4 and Nb(0.7 wt%):$SrTiO_3$ at 90 K for different currents at $H = 50$ kOe, (a) $I \leq 0.110$ mA, (b) $I > 0.110$ mA.[60]

Since the Schottky barrier varies with the electron affinity of a semiconductor, differently Nb-doped Fe_3O_4/Nb:$SrTiO_3$ heterostructures (0.5 wt%, 0.7 wt%, and 1.0 wt%) were fabricated to demonstrate the effect of barrier height on the AMR across the interface. The transport mechanism was concluded to be thermal emission for all the samples from the linear relation of $\lg|I| - V$, as shown in Fig. 20(a). The work function of Fe_3O_4 is ~ 5.3 eV.[53] The Fermi level of n-type semiconductor Nb:$SrTiO_3$ moves upward with increased doping concentration of Nb, resulting in the increase of the barrier height (the work function difference between Fe_3O_4 and Nb:$SrTiO_3$) at the interface. Consistent with that, we indeed found that the critical current, across which the 45° phase shifts were observed in the AMR for all the samples, increases with the doping content (Fig. 20(b)). The comparison of the critical bias for the maximum AMR and the calculated Schottky barrier Φ_B for different Nb doping contents is shown in Fig. 20(c), confirming that the large AMR across the interface that appears at the critical bias is closely related to the Schottky barrier.

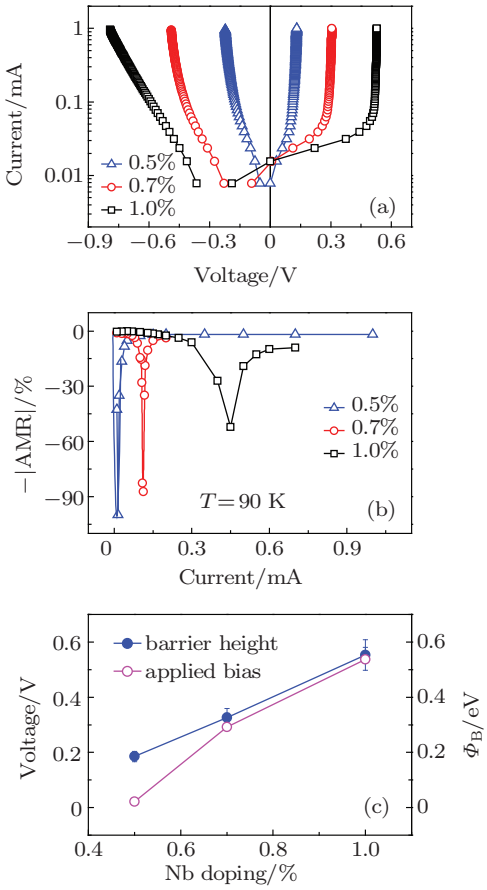


Fig. 20. (a) $\lg|I| \sim V$ relation of the Fe_3O_4/Nb:$SrTiO_3$ heterostructures with different Nb doping contents measured at $T = 90$ K. (b) Current dependence of $-|\text{AMR}|$ across interface with different Nb doping contents measured at $T = 90$ K. (c) Nb content dependence of barrier height and critical bias for maximum AMR.[60]

Therefore, the physical picture of the large four-fold AMR observed in the Fe_3O_4/Nb:$SrTiO_3$ can be explained as follows. The symmetry of the AMR across the interface in the Fe_3O_4/semiconductor heterostructures is closely related to the magnetocrystalline anisotropy of magnetite, which is decided by the SO interaction at interface. The Schottky barrier is significant for obtaining the large AMR in the heterostructures, noting that the AMR is rather small in the Ohmic contacted Fe_3O_4/ZnO heterostructure and that the critical bias for the maximum AMR in the Fe_3O_4/Nb:$SrTiO_3$ heterostructure increases with the Schottky barrier height. It has been proved that there are a lot of antiferromagnetic coupled antiphase boundaries (APBs) in epitaxial Fe_3O_4 films due to stack faults,

and they dominate the transport of electrons in epitaxial Fe_3O_4 films at high magnetic field because the spins have already been oriented except for those near the APBs.[9, 16] The Zeeman energy of the system is nearly unchanged while the magnetic field is rotating in the film plane. When the applied bias is near the height of the Schottky barrier, it is the magnetocrystalline anisotropy energy (E_K) that leads to the large sinusoidal variation of resistance because the scattering probability of electrons across the interface is enhanced while the magnetic field (50 kOe) is along the hard axis due to the frustrated alignments of the moments across the APBs and *vice versa*. According to this picture, the AMR and the effect of E_K on electron transport should be insignificant at a bias (current) much smaller or larger than the Schottky barrier, which is indeed what we observed (see Fig. 19).

The rhombohedral α-Fe_2O_3 is an antiferromagnetic insulator, and giant TMR was observed in the polycrystalline $Zn_{0.41}Fe_{2.59}O_4$ with α-Fe_2O_3 boundaries.[25] The electrical transport properties of sputtered polycrystalline Fe_3O_4/α-Fe_2O_3 heterostructures were investigated. The effect of magnetic field on the transport properties of Fe_3O_4/α-Fe_2O_3 heterostructure is shown in Fig. 21. In the insets of Fig. 21(a), the current at a fixed voltage increases as the field increases to 90 kOe, revealing that MR is negative. The MR is defined as

$$\begin{aligned} \mathrm{MR} &= \frac{R_{\mathrm{Junc}}(H\ \mathrm{kOe}) - R_{\mathrm{Junc}}(0\ \mathrm{kOe})}{R_{\mathrm{Junc}}(0\ \mathrm{kOe})} \\ &= \frac{V(H\ \mathrm{kOe}, I\ \mathrm{A}) - V(0\ \mathrm{kOe}, I\ \mathrm{A})}{V(0\ \mathrm{kOe}, I\ \mathrm{A})}. \end{aligned} \tag{9}$$

In Fig. 21(a), in the temperature range of 30 K–170 K, MR decreases with decreasing current in the high-current range and increases in the low-current range. Above 180 K, MR increases with lowering current. In Fig. 21(b), the value of negative MR reaches its minimum at 80 K. In the temperature range of 80 K–230 K, the value of negative MR increases with temperature, and reaches a maximum at 230 K, which is about −32% at 1 mA. Above 230 K, MR turns positive, and the maximum MR is about 80% measured at 1 mA at 305 K. The inset of Fig. 21(b) shows that MR at 305 K under different fields decreases with increasing current. The temperature-dependence of MR at positive and negative currents is consistent with the rectifying behavior (not shown).[61]

The present MR is different from those reported previously.[62, 63, 32] The temperature-dependent rectifying effect suggests that above 230 K the electrons escape from the Fe_3O_4 layer because electrons in Fe_3O_4 are trapped in the insulating layer at the Fe_3O_4/α-Fe_2O_3 interface due oxygen deficiency, geometric asymmetry, etc. Below 230 K, the electrons are trapped in the Fe_3O_4 layer.

For Fe_3O_4, the fivefold d levels of Fe ions occupying the octahedral sites are split into three degenerate t_{2g} levels and two degenerate e_g levels because of the crystal field splitting. At E_F, the extra electron occupies only the $t_{2g}\downarrow$ level, as is the case in region I of Figs. 22(a) and 22(b). The temperature-dependent MR is related to the rectifying effect. At low temperatures, the electrons of the Ag electrode tunnel through the α-Fe_2O_3 layer into the $t_{2g}\downarrow$ and/or $e_g\downarrow$ levels of the Fe_3O_4 layer near the Fe_3O_4/α-Fe_2O_3 interface, which makes the band structure turn to that in region II of Fig. 22(a). So when the electrons transport through the Fe_3O_4 near and far away from the barrier, the negative MR appears. The MR value is related to the spin polarization, as it is in the Fe_3O_4/Nd:$SrTiO_3$ and $Fe_3O_4/CoCr_2O_4/La_{0.7}Sr_{0.3}MnO_3$ structures.[32, 64] At high temperatures, electrons in the $t_{2g}\downarrow$ level of Fe_3O_4 are trapped into the insulating layer. With increasing temperature, more electrons are trapped into the insulating layer so the $e_g\uparrow$ band is not full, as shown in region II of Fig. 22(b). Because the electrons at the E_F of the Fe_3O_4 near the α-Fe_2O_3 barrier are spin-up (the region II of Fig. 22(b)) and the electrons at the E_F of the Fe_3O_4 far away from the barrier are spin-down (region I of Fig. 22(b)), the positive MR appears when the electrons transport though regions I and II as the magnetic field is applied. At temperatures in the range of 230 K–260 K, with increasing current, a crossover of MR from negative to positive was observed, consistent with that observed in the $Fe_3O_4/BaTiO_3$, LaCaMnO/NSTO, and LaCeMnO/NSTO structures.[65, 66, 67] The similar band structures, modulating positive and negative MR, were also observed in Fe_3O_4/p-Si, Fe_3O_4/a-C/n-Si, Fe_3O_4/MgO/Fe_3O_4, Fe_3O_4/MgO/Si, and Fe_3O_4/SiO_2/Si heterostructures.[68, 69]

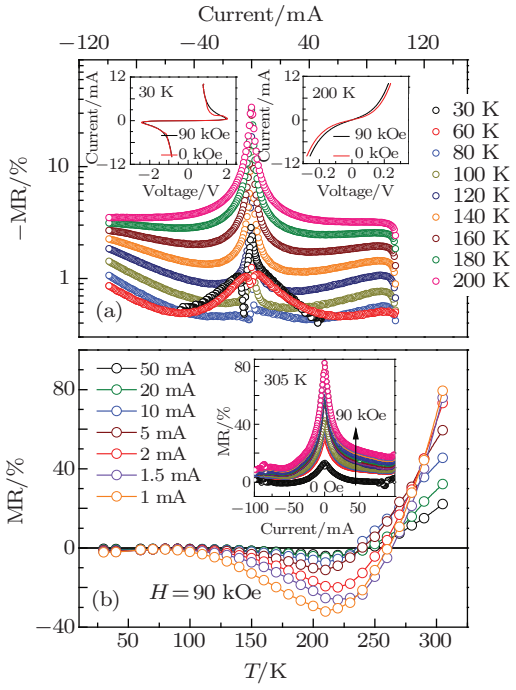


Fig. 21. (a) MR–I curves of the Fe_3O_4/α-Fe_2O_3 structures measured at different temperatures. Insets are the I–V curves measured at 0 and 90 kOe at 30 K and 200 K, respectively. (b) MR–T curves of the heterostructure measured at different currents.[61]

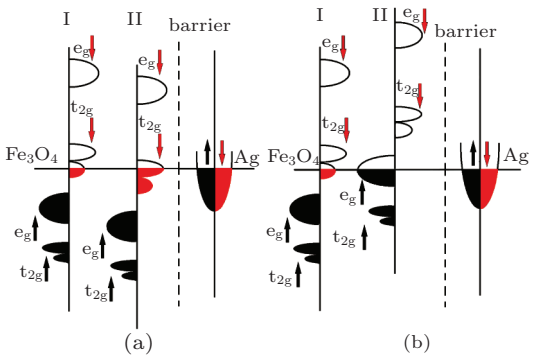


Fig. 22. Schematic density of states (DOS) of the Fe_3O_4/α-Fe_2O_3 structures: (a) when electrons diffuse into Fe_3O_4 near the barrier and negative MR appears; (b) when electrons flow away from Fe_3O_4 near the barrier and positive MR appears.[61]

Recently, multiferroic materials with ferroelectric and (anti-) ferromagnetic ordering have been shown to exhibit interesting behaviors, such as magnetoelectric,[70] magnetooptic,[71] and other exciting effects. $BiFeO_3$ (BFO) with room temperature ferroelectric and antiferromagnetic (AFM) properties[72, 73] has been widely studied. The Fe_3O_4/BFO bilayers containing multivalent transition metal ions Fe^{2+}/Fe^{3+}, similar to such manganite multilayers as Mn^{3+}/Mn^{4+},[74, 75] are expected to cause interesting phenomena with interfacial coupling.

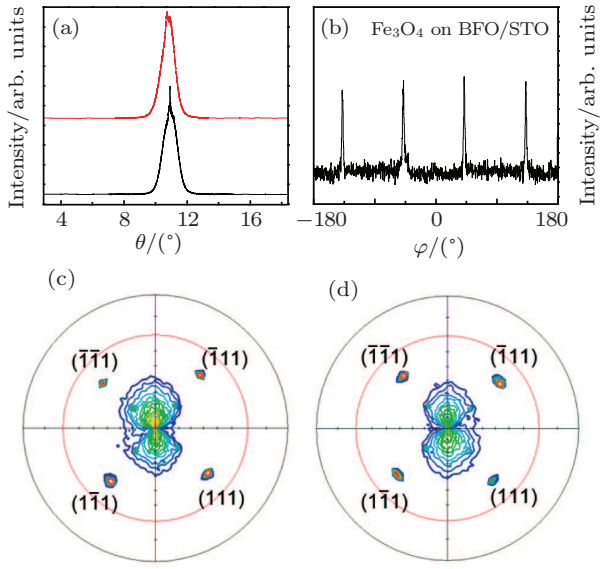


Fig. 23. XRD θ–2θ scans for single-layer films and heterostructures: (a) X-ray rocking curve (ω–θ scan) of (001) reflection of the BFO layer with (top panel) and without (bottom panel) Fe_3O_4 films; (b) φ–scan of the (220) reflection of the Fe_3O_4 film deposited on BFO layer; (c) pole figure of the epitaxial BFO single films of (222) reflection; (d) pole figure of BFO layer of (222) reflection in bilayer.[76]

The rocking curves in Fig. 23(a) give the full width at half maximum (FWHM) values of 0.79° and 0.80° for the (001) BFO reflection, corresponding to the samples with and without Fe_3O_4, respectively. The similar FWHM values imply that the crystallinity of the BFO layer is not affected by the deposition of Fe_3O_4. Figure 23(b) shows the $\{111\}$ φ–scan of the epitaxial Fe_3O_4 films on top of BFO, and Figs. 23(c) and 23(d) give the corresponding $\{111\}$ pole figures of the BFO layer without and with Fe_3O_4, respectively. Four strong diffraction peaks indicate that the epitaxial structure of BFO layer is also not disturbed by the deposition of epitaxial Fe_3O_4 films.

Figure 24(a) shows that $M_u(Fe_3O_4/BFO)$ varies significantly with the thickness of BFO (t_{BFO}). $M_u(t_{BFO}=0)$ corresponds to the moment of the Fe_3O_4 monolayer. Figure 24(b) displays the thickness-dependent moments of BFO monolayer and the BFO layers in the bilayers with the contribution of Fe_3O_4 films subtracted. M_u increases with decreasing t_{BFO} in the bilayers. We suppose that the Fe_3O_4 films have the same magnetization in all the samples due to their identical deposition conditions and similar lattice mismatch revealed by XRD results (not shown), so the remaining magnetization of the bilayers can be expressed as

$$M = M_S(\mathrm{BFO}) + M_i, \tag{10}$$

where $M_S(\mathrm{BFO})$ stands for the saturation magnetization of the BFO films and M_i is the additional magnetization contribution from the coupling interface.

As shown in Fig. 24(b), the magnetization of 22-nm BFO layer is unexpectedly large (456 emu/cm^3) compared to BFO monolayer (57 emu/cm^3). To explain the significant enhancement, the critical step is to consider the interface terminations. In the (001) plane, $BiFeO_3$ is composed of alternating FeO and BiO_2 layers, while Fe^A and $Fe_2^BO_4$ layers alternate in Fe_3O_4.[74] Considering the principle of lower interface energy[77] and bismuth's volatile nature at the BFO surface, the most stable interface structure in the Fe_3O_4/BFO bilayers should be $[Fe_2^BO_4]^{3-}/[FeO]^+$.

The electronic orbital reconstruction at the interface has been introduced in many reports.[74, 75, 78, 79] First, based on the interface structure $[Fe_2^BO_4]^{3-}/[FeO]^+$, the magnetic interaction of the Fe ions must be determined by the competition between DE and superexchange. Compared to superexchange via Fe t_{2g} electrons, much stronger DE between $d_{3z^2-r^2}$ orbitals of Fe e_g (Fe_3O_4 and BFO) via oxygen $2p_z$ orbitals will be dominant for reconstruction.[17, 80] The Fe^{2+} in Fe_3O_4 films at the interface is replaced by Fe^{3+} from the BFO layer through DE. To maintain charge balance, it is likely that the Fe^{3+} on an A site changes to Fe^{2+}, forming normal spinel structures (6 μ_B/f.u.) in which the moment is much larger than that of inverse spinel Fe_3O_4 films (4 μ_B/f.u.).[81]

Second, the magnetization of the Fe_3O_4 films does not saturate for existence of APBs.[16, 17, 80] The boundaries are predominantly composed of the segments on $\{110\}$ planes,[16, 17, 80] and the other moments far from APBs are aligned along the field in (001) plane. In the (001) plane of BFO films, some of the magnetic moments align along $\langle 110\rangle$ ferromagnetically, and others are parallel to the AFM order

along other directions.[82] In the bilayers, as shown in the schematic diagram in Fig. 24(c), the AFM moments near the interface will decrease under the induction of the ferromagnetic order from both phases because of interfacial ferromagnetic coupling under the applied field.

As for the decreasing trend of moment with t_{BFO} in Fig. 24, a possible mechanism is a gradual increase in the canting angle as the thickness decreases, which could be driven by increasing distortions due to epitaxial strain.[83] Therefore, the coupling would be stronger for the thinner BFO films.

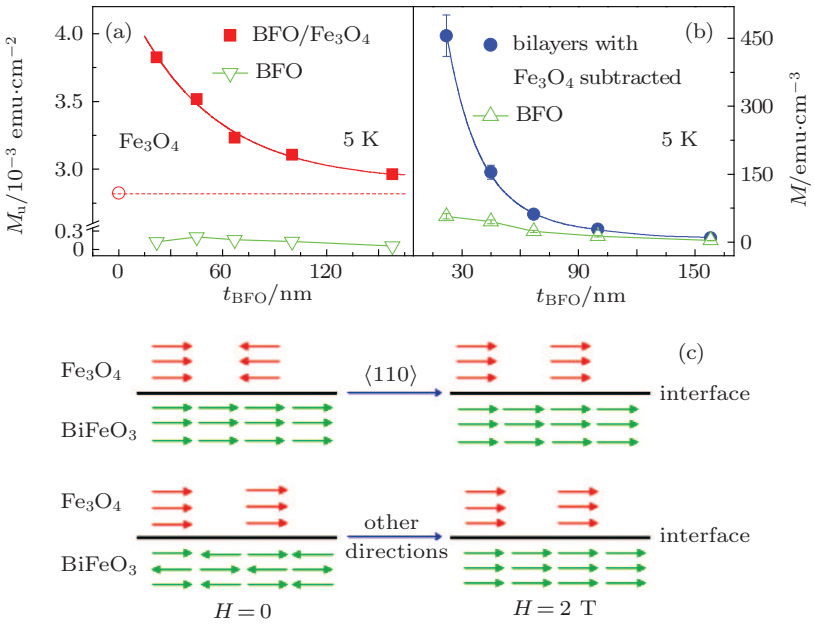


Fig. 24. (a) Total magnetic moments of different samples measured at 5 K as a function of t_{BFO}. (b) Magnetic moment of the Fe_3O_4/BFO heterostructures subtracting the contribution of Fe_3O_4 films with error bars. Triangle connection line is the contribution of the BFO single-layer. (c) Schematic diagram of the interface coupling effect.[76]

Experimentally, the enhanced magnetization and exchange bias have been observed in the Fe_3O_4/BFO bilayers. In order to investigate the mechanism of the interfacial magnetic coupling, the magnetic coupling of Fe_3O_4/BFO(001) superlattices consisting of Fe_3O_4 and tetragonal phase BFO with large spontaneous electric polarization were investigated by first principles calculations. Two models were investigated, with model (a) containing the Fe(A)–BiO and Fe_2O_4(B)–FeO_2 interfaces and model (b) containing the Fe(A)–FeO_2 and Fe_2O_4(B)–BiO interfaces. The calculation gives magnetization enhancements of 13% and 8% for models (a) and (b), respectively.[84]

6. Outlook

The fundamental magnetic and transport properties of half-metallic Fe_3O_4 films and Fe_3O_4-based heterostructures, which are beneficial for their practical applications in spintronics, have been illustrated. Recently, multiferroic materials have attracted great attention, especially for the interfacial magnetic coupling between magnetic and ferroelectric materials. The interfacial magnetic coupling in the heterostructures combined with Fe_3O_4 and other ferroelectric films will be pursued for future spintronic applications.

References

[1] Verwey J E W and Haayman P W 1941 *Physica* **8** 979
[2] Zhang Z and Satpathy S 1991 *Phys. Rev. B* **44** 13319
[3] Hu G and Suzuki Y 2002 *Phys. Rev. Lett.* **89** 276601
[4] Zhao L B, Mi W B, Jiang E Y and Bai H L 2007 *Appl. Phys. Lett.* **91** 052113
[5] Tripathy D, Adeyeye A O and Shannigrahi S 2007 *Phys. Rev. B* **75** 012403
[6] Mitani S, Takahashi S, Takanashi K, Yakushiji K, Maekawa S and Fujimori H 1998 *Phys. Rev. Lett.* **81** 2799
[7] Li X W, Gupta A, Xiao G, Qian W and Dravid V P 1998 *Appl. Phys. Lett.* **73** 3282
[8] Inoue J and Maekawa S 1996 *Phys. Rev. B* **53** R11927
[9] Eerenstein W, Palstra T T M, Saxena S S and Hibma T 2002 *Phys. Rev. Lett.* **88** 247204
[10] Eerenstein W, Palstra T T M, Hibma T and Celotto S 2002 *Phys. Rev. B* **66** R20110
[11] Coey J M D, Berkowitz A E, Balcells L, Putris F F and Parker F T 1998 *Appl. Phys. Lett.* **72** 734
[12] Coey J M D, Berkowitz A E, Balcells L, Putris F F and Barry A 1998 *Phys. Rev. Lett.* **80** 3815
[13] Peng D L, Asai T, Nozawa N, Hihara T and Sumiyama K 2002 *Appl. Phys. Lett.* **81** 4598
[14] Gridin V V, Hearne G R and Honig J M 1996 *Phys. Rev. B* **53** 15518
[15] Wawatzky G A, Geertsma W and Haas C 1976 *J. Magn. Magn. Mater.* **3** 37
[16] Margulies D T, Parker F T, Rudee M L, Spada F E, Chapman J N, Aitchison P R and Berkowitz A E 1997 *Phys. Rev. Lett.* **79** 5162
[17] Margulies D T, Parker F T, Spada F E, Goldman R S, Li J, Sinclair R and Berkowitz A E 1996 *Phys. Rev. B* **53** 9175
[18] Hammar P R, Bennett B R, Yang M J and Johnson M 1999 *Phys. Rev. Lett.* **83** 203
[19] Schmidt G, Ferrand D, Molenkamp L W, Filip A T and van Wees B J 2000 *Phys. Rev. B* **62** R4709

[20] Rashba E I 2000 *Phys. Rev. B* **62** R16267
[21] Fert A and Jaffrès H 2001 *Phys. Rev. B* **64** 184420
[22] Ohno Y, Young D K, Beschoten B, Matsukura F, Ohno H and Awschalom D D 1999 *Nature* **402** 790
[23] Watts S M, Nakajima K, van Dijken S and Coey J M 2004 *J. Appl. Phys.* **95** 7465
[24] Watts S M, Boothman C, van Dijken S and Coey J M 2005 *Appl. Phys. Lett.* **86** 212108
[25] Chen P L, Xing D Y, Du Y W, Zhu J M and Feng D 2001 *Phys. Rev. Lett.* **87** 107202
[26] Mi W B, Shen J J, Jiang E Y and Bai H L 2007 *Acta Mater.* **55** 1919
[27] Liu H, Jiang E Y, Bai H L, Zheng R K, Wei H L and Zhang X X 2003 *Appl. Phys. Lett.* **83** 3531
[28] Shepherd J P, Koenitzer J W, Aragon R, Spalek J and Honig J M 1991 *Phys. Rev. B* **43** 8461
[29] Arora S K, Sofin R G S, Nolan A and Shvets I V 2005 *J. Magn. Magn. Mater.* **286** 463
[30] Zheng R K, Wen G H, Fung K K and Zhang X X 2004 *Phys. Rev. B* **69** 214431
[31] Chien C L, Xiao J Q and Jiang J S 1993 *J. Appl. Phys.* **73** 5309
[32] Li P, Zhang L T, Mi W B, Jiang E Y and Bai H L 2009 *J. Appl. Phys.* **106** 033908
[33] Li P, Jiang E Y and Bai H L 2010 *J. Phys. D: Appl. Phys.* **43** 265002
[34] Li P, Jin C, Jiang E Y and Bai H L 2010 *J. Appl. Phys.* **108** 093921
[35] Helman J S and Abeles B 1976 *Phys. Rev. Lett.* **37** 1429
[36] Degiorgi L, Wachter P and Ihle D 1987 *Phys. Rev. B* **35** 9259
[37] Ziese M, Hohne R, Semmelhack H C, Reckentin H, Hong N H and Esquinazi P 2002 *Eur. Phys. J. B* **28** 415
[38] Eerenstein W, Palstra T T M, Hibma T and Celotto S 2003 *Phys. Rev. B* **68** 014428
[39] Bickford L R 1950 *Phys. Rev.* **78** 449
[40] Palmer W 1963 *Phys. Rev.* **131** 1057
[41] Li P, Jiang E Y and Bai H L 2010 *Appl. Phys. Lett.* **96** 092502
[42] Ramos R, Arora S K and Shvets 2008 *Phys. Rev. B* **78** 214402
[43] Venzke S, van Dover R B, Phillips J M, Gyorgy E M, Siegrist T, Chen C H, Werder D, Fleming R M, Felder R J, Coleman E and Opila R 1996 *J. Mater. Res.* **11** 1187
[44] Chakraverty S, Mitra S, Mandal K, Nambissan P M G and Chattopadhyay S 2005 *Phys. Rev. B* **71** 024115
[45] Li P, Sun M Y, Jin C and Bai H L 2012 *J. Phys. D: Appl. Phys.* **45** 505001
[46] Jin C, Li P, Mi W B and Bai H L 2012 *Europhys. Lett.* **100** 27006
[47] Penoyer R F and Bickford L R 1957 *Phys. Rev.* **108** 271
[48] Bozorth R M, Tilden E F and Williams A J 1955 *Phys. Rev.* **99** 1788
[49] Snyder G J, Hiskers R, Dicarolis S, Beasley M R and Geballe T H 1996 *Phys. Rev. B* **53** 14434
[50] Walter T, Dorr K, Muller K H, Eckert D, Nenkov K, Hecker M, Lehmann M and Schultz L 2000 *J. Magn. Magn. Mater.* **222** 175
[51] Ohta H, Kawamura K, Orita M, Hirano M, Sarukura N and Hosono H 2000 *Appl. Phys. Lett.* **77** 475
[52] Hwang D, Kang S H, Lim J H, Yang E J, Oh J Y, Yang J H and Park S J 2005 *Appl. Phys. Lett.* **86** 222101
[53] Bamiduro O, Mustafa H, Mundle R, Konda R B and Pradhan A K 2007 *Appl. Phys. Lett.* **90** 252108
[54] Dietl T, Ohno H, Matsukura F, Cibert J and Ferrand D 2000 *Science* **287** 1019
[55] Nielsen A, Brandlmaier A, Althammer M, Kaiser W, Opel M, Simon J, Mader W, Goennenwein S T B and Gross R 2008 *Appl. Phys. Lett.* **93** 162510
[56] Ozgur U, Alivov Y I, Liu C, Teke A, Reshchikov M A, Dogan S, Avrutin V, Cho S J and Morkoc H 2005 *J. Appl. Phys.* **98** 041301
[57] Sze S M 1981 *Physics of Semiconductor Devices* (New York: Wiley)
[58] Ziese M, Köhler U, Bollero A, Höhne R and Esquinazi P 2005 *Phys. Rev. B* **71** 180406
[59] Li P, Guo B L and Bai H L 2011 *J. Appl. Phys.* **109** 013908
[60] Li P, Guo B L and Bai H L 2011 *Europhys. Lett.* **94** 57007
[61] Mi W B, Jiang E Y and Bai H L 2008 *Appl. Phys. Lett.* **93** 132504
[62] Qu T L, Zhao Y G, Tian H F, Xiong C M, Guo S M and Li J Q 2007 *Appl. Phys. Lett.* **90** 223514
[63] Chen Y F and Ziese M 2007 *J. Phys. D: Appl. Phys.* **40** 3271
[64] Hu G and Suzuki Y 2002 *Phys. Rev. Lett.* **89** 272002
[65] Yanase Y and Siratori K 1984 *J. Phys. Soc. Jpn.* **53** 312
[66] Zhou T F, Li G, Wang N Y, Wang B M, Lia X G and Chen Y 2006 *Appl. Phys. Lett.* **88** 232508
[67] Sheng Z G, Song W H, Sun Y P, Sun J R and Shen B G 2005 *Appl. Phys. Lett.* **87** 032501
[68] Fan Z W, Li P, Zhang L T, Mi W B, Jiang E Y and Bai H L 2012 *Thin Solid Films* **520** 3641
[69] Zhang L T, Li P, Mi W B and Bai H L 2012 *J. Magn. Magn. Mater.* **324** 3731
[70] Eerenstein W, Mathur N D and Scott J F 2006 *Nature* **442** 759
[71] Kanai T, Ohkoshi S I, Nakajima A, Watanabe T and K Hashimoto 2001 *Adv. Mater.* **13** 487
[72] Wang J, Neaton J B, Zheng H, Nagarajan V, Ogale S B, Liu B, Viehland D, Vaithyanathan V, Schlom D G, Waghmare U V, Spaldin N A, Rabe K M, Wuttig M and Ramesh R 2003 *Science* **299** 1719
[73] Yang S Y, Zavaliche F, Mohaddes-Ardabili L, Vaithyanathan V, Schlom D G, Lee Y J, Chu Y H, Cruz M P, Zhan Q, Zhao T and Ramesh R 2005 *Appl. Phys. Lett.* **87** 102903
[74] Yu R, Yunoki S J, Dong S and Dagotto E 2009 *Phys. Rev. B* **80** 125115
[75] Yu P, Lee J S, Okamoto S, Rossell M D, Huijben M, Yang C H, He Q, Zhang J X, Yang S Y, Lee M J, Ramasse Q M, Erni R, Chu Y H, Arena D A, Kao C C, Martin L W and Ramesh R 2010 *Phys. Rev. Lett.* **105** 027201
[76] Liu X F, Li P, Jin C and Bai H L 2011 *Appl. Phys. Lett.* **99** 182511
[77] Zhan Q, Yu R, Crane S P, Zheng H, Kisielowski C and Ramesh R 2006 *Appl. Phys. Lett.* **89** 172902
[78] Baena A, Brey L and Calder'on M J 2011 *Phys. Rev. B* **83** 064424
[79] Niebieskikwiat D, Hueso L E, Borchers J A, Mathur N D and Salamon M B 2007 *Phys. Rev. Lett.* **99** 247207
[80] Rudee M L, Margulies D T and Berkowitz A E 1997 *Microsc. Microanal.* **3** 126
[81] Lüders U, Bibes M, Bobo J F, Cantoni M, Bertacco R and Fontcuberta J 2005 *Phys. Rev. B* **71** 134419
[82] Lebeugle D, Colson D, Forget A, Viret M, Bataille A M and A Gukasov 2008 *Phys. Rev. Lett.* **100** 227602
[83] Wang J, Scholl A, Zheng H, Ogale S B, Viehland D, Schlom D G, Spaldin N A, Rabe K M, Wuttig M, Mohaddes L, Neaton J, Waghmare U V, Zhao T and Ramesh R 2005 *Science* **307** 1203
[84] Yang H, Jin C, Mi W B and Bai H L 2012 *J. Appl. Phys.* **112** 063925